PNAS

Main Manuscript for

Discovery of Polarized Twin Walls in a Halide Perovskite

Weilun Li[1], Qimu Yuan[2], Michael B. Johnston[2], Joanne Etheridge[1,3,4*]

[1] School of Physics and Astronomy, Monash University, Victoria, 3800, Australia

[2] Department of Physics, University of Oxford, Oxford OX1 3PU, United Kingdom

[3] Monash Centre for Electron Microscopy, Monash University, Victoria, 3800, Australia

[4] Department of Materials Science and Engineering, Monash University, Victoria, 3800, Australia

* Joanne Etheridge

Email: joanne.etheridge@monash.edu

Author Contributions: W.L. and J.E. conceived and designed the project. W.L. carried out TEM experiments and analyzed data under the supervision of J.E.. Q.Y. optimized and prepared specimens under the supervision of M.B.J.. W.L. and J.E. prepared the manuscript. All authors contributed to the discussion of the results and revision of the manuscript.

Competing Interest Statement: The authors declare no competing interests.

Classification: Physical Sciences/Applied Physical Sciences; Physical Sciences/Engineering Sciences

Keywords: Halide Perovskites; Solar Cells; Electron Microscopy; Structure-Property Relationships

This PDF file includes:

Main Text
Figures 1 to 5

Abstract

Halide perovskites have emerged as promising materials for next-generation photovoltaics, laser sources and X-ray detectors. There is intense debate as to whether some photoactive halide perovskites exhibit ferroelectric behavior and whether it might be possible to utilize the bulk photovoltaic effect to enhance the performance of halide perovskite solar cells. Here, using low-dose scanning transmission electron microscopy, we discover the existence of ferroelastic twin walls in vapor-deposited $CsPbI_3$ thin films, parallel to {110} and {112}. Remarkably, despite $CsPbI_3$ being centrosymmetric and non-polar, we observe directly that Pb atoms shift at {110} twin walls driving a local ferroelectric-like polarization. These polar twin walls form an intrinsic array of nanoscale interfaces, spaced ~30-50 nm apart, embedded within the non-polar perovskite lattice. In contrast, {112} twin walls do not show a polar displacement of Pb but strongly suppress octahedral tilt and off-center Cs atom displacements, revealing a different untapped structural degree of freedom. These discoveries together uncover previously hidden nanoscale polarization in halide perovskite semiconductors, opening opportunities for enhanced conductivity and photovoltaic behavior through domain wall engineering.

Significance Statement

Halide perovskites are leading materials for solar cells and light-emitting devices, yet whether they exhibit useful ferroelectric functionality has remained unresolved. This work provides direct atomic-scale evidence that nominally non-polar $CsPbI_3$ hosts polarized ferroelastic twin walls. Confined to just a few atomic layers, these polar domain walls spontaneously form a periodic array of polarized nanodomains embedded within the otherwise non-polar semiconductor, opening the possibility of ferroelectric-behavior. This discovery identifies an additional structural element in halide perovskites that could be engineered, analogous to successful approaches developed in oxide ferroics.

Main Text

Introduction

Metal halide perovskite (MHPs) semiconductors have attracted intense interest for high-performance, low-cost solar cells[1], lasers[2], light-emitting diodes[3], and photodetectors[4]. A defining feature of the perovskite structure is its ability to host a rich variety of ferroic phenomena, such as ferroelectricity, ferroelasticity, flexoelectricity, enabled by its structurally flexible lattices and propensity to break inversion symmetry[5,6].

In oxide perovskites, ferroic properties and associated domains underpin functional responses that can be engineered to enhance material performance[7,8]. Establishing whether analogous ferroic behavior exists in halide perovskite is therefore important, particularly for solar cells, where internal electric fields from polar or charged domain or domain walls could influence In particular, in solar cells, the ferroelectric effect can influence bulk photovoltaic effect (BPVE)[9], conductivity[7,10] and charge separation[11].

In halide perovskites, however, ferroic behavior is nascent, with relatively few studies investigating the possible existence of ferroic properties. Ferroelastic domains have been observed in certain systems, such as $CsPbBr_3$[12–14] and $MAPbI_3$[15–17], however, there remains intense debate as to whether ferroelectricity exists in these, or indeed any other, halide perovskite semiconductor[17–21]. A key challenge is determining crystal symmetry and domain structures at the relevant length

scales[17,22] while avoiding structural degradation. X-ray diffraction (XRD), electron diffraction, and piezo-response force microscopy (PFM) have revealed mesoscale domain patterns in several halide perovskites[13,15,16,18,23], but these various observations have been interpretated variously as arising from polarization[18,23], spontaneous strain[13,15,16] or compositional inhomogeneity[17]. Such methods generally lack the spatial resolution needed to directly resolve atomically thin domain walls or local symmetry breaking. Atomic-resolution transmission electron microscopy (TEM) could provide atomic insights into ferroic domain walls, as in oxide perovskites[24]; however, the extreme electron beam sensitivity of halide perovskites poses a significant obstacle to achieving quantitative structural information at the atomic level[25–28]. Consequently, direct atomic-scale evidence of ferroelastic domains in halide perovskites remains scarce[12–14]. Furthermore, there has, as yet, been no atomic-scale evidence of ferroelectric domains.

All-inorganic $CsPbX_3$ (where X = I^-, Br^- or Cl^-) have attracted increasing interest due to their remarkable optoelectronic properties combined with improved environmental stability compared to hybrid organic-inorganic counterparts[29]. By replacing volatile organic cations with inorganic Cs^+, these materials avoid organic cation related decomposition pathways and thereby reduce volatility under thermal or chemical stress[30,31]. It has been proposed that the lone pair on Pb^{2+} cations can lead to ferroelectricity in $CsPbX_3$ through Pb off-center displacements[32,33] and nanoscale ferroelectricity has been predicted theoretically[34]. However, apart from a report of a polar orthorhombic phase in $CsPbBr_3$ quantum dots at freezing temperatures (space group: *Pna2₁* below 263K)[35] (see SI, supplementary note 5), the majority of research on bulk and thin-film $CsPbX_3$ has reported an orthorhombic phase (γ-phase) at room temperature with a centrosymmetric, hence non-polar, structure (space group: *Pnma/Pbnm)*[36,37].

In $CsPbI_3$, whose bandgap is well suited for intrinsic absorber in both single-junction and multi-junction photovoltaic devices, local structural investigations are limited owing to its extreme phase instability. To the best of our knowledge, no twin domains, let alone ferroelectric domains, have been reported[38,39].

Here, we use low-dose atomic-resolution TEM to probe $CsPbI_3$ thin films prepared by vapor co-deposition following our previously optimized protocol for TEM characterization (details in methods and supplementary note 5)[39]. Remarkably, we discover the existence of ferroelastic twin domains which have polar domain walls, introducing the possibility of localized ferroelectricity. These twin domains and walls have a completely different structure compared with those observed in $CsPbBr_3$[12–14] and $MAPbI_3$[15–17]. Specifically, while we confirm that the domain interiors of orthorhombic $CsPbI_3$ thin films are non-polar, we reveal that it contains two types of twin domains along {110} and {112} planes. Quantitative analysis of symmetry, strain, and local atomic positions reveals Pb displacement at {110} twin walls, forming 2-4 unit cells wide polarized domain walls that repeat at ~30-50nm intervals within each grain. By contrast, {112} twin walls do not exhibit such polar displacement of Pb; instead, they are characterized by relaxation of the octahedral tilts and Cs off-center displacements. Our results provide direct atomic-scale evidence for polarized domain walls in $CsPbI_3$. These walls occur at regular intervals within the non-polar matrix, with the potential to act, or be engineered, as nanoscale functional elements.

Results

Non-polar domain interiors in $CsPbI_3$

We began our study by determining the crystal structure, symmetry and polarity within $CsPbI_3$ grains. Thin films of $CsPbI_3$ were prepared by thermal vapor co-deposition, a solvent-free, scalable technique widely used for fabricating high-quality MHP devices[40,41]. The deposited thin film exhibits a uniform and reproducible microstructure across the TEM specimen (**Fig. S1**).

Using annular dark field scanning transmission electron microscopy (STEM-ADF), we imaged the atomic structure and measured the positions of atomic columns (**Fig. 1(C-J)**), keeping electron dose as low as possible (see Methods). From atomic-resolution STEM-ADF images along multiple zone axes, we confirm that $CsPbI_3$ adopts an orthorhombic perovskite structure, commonly referred to as γ-$CsPbI_3$. The diffraction patterns further confirm the formation of γ-phase and indicate a film thickness is close to the nominal value of 35 nm (**Fig. S2-S3**). We quantitatively analyzed Pb and Cs atom positions and found no detectable Pb off-center displacements anywhere in the single-crystal regions away from domain walls, confirming there is no spontaneous polarization in the domain interiors (**Fig. S4**). Consistent with the γ-$CsPbI_3$ phase, Cs shows anti-polar off-center displacements, that is, Cs atoms on adjacent A-sites shift in opposite directions along the [001] direction (**Fig. S5**). These antipolar displacements, which arise from octahedral tilts rather than spontaneous polarization, stabilizes the octahedral-tilted perovskite structure[42].

Taken together, our quantitative analyses are consistent with the domain interiors of orthorhombic $CsPbI_3$ exhibiting a non-polar, centrosymmetric structure. No evidence of Pb off-centering was detected, consistent with the centrosymmetry of the Pb-I octahedra in the *Pbnm* phase and previous reports based on macroscopic XRD refinements[36].

This phase exhibits in-phase octahedral tilts along the long axis (c-axis) and out-of-phase tilts along the other two orthogonal axes, resulting in a distorted Pb-I octahedral network (**Fig. 1A**). These octahedral tilts lead to distinct lattice parameters (*a, b, c*) along the three orthogonal axes and characteristic non-equal axes compared to the high-symmetry phases, approximately satisfying: $a_{ortho} \approx b_{ortho} \approx \sqrt{2}a_c$ and $c_{ortho} \approx 2a_c$, where "ortho" and "c" refer to orthorhombic and cubic unit cells, respectively (**Fig. 1B**).

{110} Ferroelastic Twin Domains

We next extended our structural investigation to twin domains and twin walls. To the best of our knowledge, direct observations of twin walls have not been reported previously in $CsPbI_3$. A TEM overview image (**Fig. 2A**) reveals a homogeneous grain structure with grain sizes ranging from ~100-200 nm. Notably, some grains exhibit a distinctive "stripe contrast", dividing individual grains into two or more subdomains (additional overview images are shown in **Fig. S6**).

Fig. 2B shows a grain viewed along the [001] zone axis, where intra-grain domains are clearly visible, with typical widths of ~30-50 nm. The corresponding Fourier Transform (FT) of the domain region (**Fig. 2C**) exhibits characteristic "double spots" or "twinned spots" (highlighted in **Fig. 2D**), which is a well-known signature of crystallographic twinning in perovskite materials[16,44].

Across the twin wall, the crystal lattice is mirrored, corresponding to an interchange of the a- and b- axes relative to the (110) twin plane. Since the b-axis is slightly longer than the a-axis, this interchange produces two distinct reciprocal lattice spots, one from each of the two twinned domains: the spots coincide along the twin axis but are spatially offset elsewhere, as is clearly resolved in the FT pattern. The axes interchange results in a lattice rotation across the twin wall at about 3° (i.e. 87° if considering the axis swap) measured from the angle between the spots in **Fig. 2D** and diffraction patterns in **Fig. S13H**. This angle is consistent with the lattice spacing ratio of $b/a \approx 1.03$. This can be analyzed with geometric phase analysis (GPA), which highlights the crystal rotation induced by twinning, as shown in **Fig. 2E**. Apart from lattice vector rotation across domains and the highly localized atomic-position shifts at the domain walls, no measurable internal strain is detected across the grain nor within the domain interiors (**Fig. 2E**), and the measured lattice parameters are consistent with those of bulk γ-$CsPbI_3$ (**Fig. S2** and **Fig. S8**).

The crystallography of the {110} twin wall in $CsPbI_3$ is illustrated schematically in **Fig. 2F**, along with the geometry of the corresponding diffraction patterns in **Fig. 2G**. These twin walls delineate

a switch between crystal orientation (described as A-type domains and B-type domains in **Fig. 1**) and are indicative of ferroelastic behavior in perovskite materials[45,46].

Localized Polarization at {110} Twin Walls

We have shown that orthorhombic $CsPbI_3$ adopts a centrosymmetric structure consistent with the reported *Pbnm* space group. However, we find that this inversion symmetry can be locally broken at and near the twin walls, introducing structural degrees of freedom that are absent in the regions away from the twin walls, which we describe here.

A representative region containing a {110} twin wall is shown in **Fig. 3A**. The interchange of crystallographic axes across the wall is evident from local measurements of Pb-Pb interatomic distances (corresponding to the *a* and *b* lattice parameter), as quantified in **Fig. 3B**. These structural changes confirm the presence of a (110) twin wall and are fully consistent with the crystallographic model described earlier in **Fig. 1**. Importantly, this analysis also allows us to pinpoint the precise location of the twin wall, which is challenging to discern directly from the low-dose TEM image due to subtle intensity variations.

To measure the local atomic positions at the twin wall, we analyzed the position of Pb/I columns relative to the geometric center of their surrounding I columns (**Fig. 3C**) as described in Methods. Strikingly, we observed significant off-center displacements of the Pb/I atomic columns localized at the twin wall, with the displacement vector predominantly parallel to [110], along the wall plane. These displacements are confined to a narrow region approximately four atomic layers wide (2 layers each side of the wall), indicating that the wall itself hosts a distinct structural configuration which is polar. No evidence of polarization was found within the domain interiors, confirming that they retain the non-polar character expected for the domain interiors. This polar structure differs from the previously reported polar $Pna2_1$ phase[47], in which Pb displacement occurs along the [001] direction. Because the structure varies unit-cell by unit-cell approaching and across the domain wall, it is not appropriate to assign a conventional space group to the domain-wall region, as space-group symmetry is a property of periodic crystals.

To further quantify this behavior, we resolved the Pb displacements into components parallel and perpendicular to the twin wall and plotted their magnitudes in **Fig 3D**. While minor background variations arising from measurement noise, local crystal bending, slight beam damage and slight off-axis tilt are observed, a pronounced increase in displacement is evident at the twin wall, relative to the interior (as demonstrated in **Fig. S9**-**S12**). The peak magnitude of the displacement reaches ~ 15 pm at the twin wall, clearly distinguishing it from the surrounding domains, where displacements remain negligible.

{112} Ferroelastic Twin Walls

We also identified a second type of twin wall in $CsPbI_3$ films, orientated parallel to the {112} plane. These {112} twin walls are observed only occasionally, likely due to the strong [001]-preferred grain orientation in vapor-deposited $CsPbI_3$ films. In other words, they may occur more frequently than observed but we cannot see them due to the preferred grain orientation.

The {112} twins involve an interchange of the [110] and [001] crystallographic directions across the wall (as opposed to the [100] and [010] directions for the {110} twin walls). **Fig. 4A** shows a [110]-orientated grain investigated using low dose four-dimensional STEM (4D-STEM) (see Methods). The grain is divided into two sub-domains by a twin wall parallel to the (112) plane. Notably, the diffraction patterns from either side of the wall (**Fig. 4B** and **4C**) exhibit a clear mirror symmetry in

the arrangement of diffraction spots, reflecting the interchange of crystallographic axes across the twin wall. A comparison of 4D-STEM results for the two types of twins is provided in **Fig. S13**.

An atomic-resolution STEM-ADF image of a typical {112} twin wall is shown in **Fig. 4D**. Interestingly, no measurable displacement of the Pb/I columns relative to the centers of the surrounding octahedra is observed (**Fig. 4E**), indicating the absence of localized polarization from Pb at {112}-type twin walls, in contrast to the polar distortion observed at the {110} twin wall. Analysis of Cs positions reveals pronounced anti-polar displacements in the interior of the domain, as expected for the non-polar *Pbnm* space group (**Fig. 4F**). Importantly, however, we observe that these Cs displacements reduce significantly in magnitude within the transition region at the wall.

This suppression of Cs atomic displacements at the {112} twin wall occurs together with the suppression of octahedral tilts at the wall, as evidenced by measurements of the "ellipticity" of the intensity maxima associated with the Pb/I columns (**Fig. 4G**). Together, these results suggest that, while the {112} twin walls preserve the centrosymmetry of the Pb-I framework, they reduce the antipolar displacements of Cs and the octahedral tilt to accommodate the structural reflection between the adjacent twin domains.

Discussion

In this study, we discovered and characterized two distinct types of ferroelastic twin walls in orthorhombic $CsPbI_3$, each involving an interchange between two orthogonal crystallographic axes: [100]/[010] for the {110}-type twins and [110]/[001] for the {112}-type twins. As $CsPbI_3$ cools from high temperature, it undergoes a sequence of symmetry-lowering phase transitions from cubic to tetragonal and finally to an orthorhombic phase at room temperature, accompanied by octahedral tilts and spontaneous strain[37,38]. In other perovskite compounds, such phase transitions have been shown to promote the formation of ferroelastic twin domains as a mechanism to minimize elastic energy and accommodate these structural changes[44,46].

Our quantitative atomic-resolution STEM-ADF measurements reveal no evidence of spontaneous polarization in single crystal $CsPbI_3$, within the interior of either type of twin domain, indicating the absence of polarization in the domain interiors in $CsPbI_3$, consistent with its reported space group Remarkably, however, we find that these ferroelastic twin wall can locally break inversion symmetry and host polar distortions, despite the centrosymmetric, non-polar nature of the surrounding interior matrix. This phenomenon is clearly observed at {110}-type twin walls (**Fig. 5(A, C)**).

Polar ferroelastic domain walls have previously been observed and/or predicted in oxide perovskites such as $CaTiO_3$[48], $SrTiO_3$[49], $GdFeO_3$[50] and have been predicted theoretically in $CsPbI_3$[51], establishing a microscopic theoretical framework for understanding twin-wall induced polarization. This work provides the first direct experimental evidence of such polar domain walls in a photoactive halide perovskite, demonstrating they are not exclusive to oxide perovskites. This opens some exciting possibilities in analogy with the oxide perovskites where domain wall functionalities[7,8] have already enabled novel device concepts including diodes[52], memories[53] and tunnel junctions[54].

The polarization vectors are consistently oriented parallel to the twin wall, a characteristic shared with the polar domain walls in the oxide perovskite systems. The spatial extent of the polar region, confined to approximately four atomic layers, also aligns well with theorical predictions for $CaTiO_3$[55]. Our measurements show that the B-site cations (Pb^{2+}) are displaced by up to ~ 15 pm at the {110} twin walls. This displacement is more than twice that observed for B-site displacement in $CaTiO_3$ (~ 6 pm)[48] but smaller than the A-site polar displacement in $GdFeO_3$ (~ 30 pm)[50]. The 15 pm Pb displacement relative to the lattice away from the wall can be converted into a projected polarization P_s with the equation $P_s = \frac{1}{V}\sum \delta_i Z_i$, where V is the volume of unit cell, δ_i is the displacement, and Z_i

is the Born effective charge of atom i [56]. This yields an estimated polarization of 4.35 μC cm^{-2} and an ideal unscreened field of 8.6 x 10^8 V/m, using Z_{Pb} = 4.42 and a dielectric constant ϵ = 5.70, obtained from density functional theory for locally distorted, polymorphous $CsPbI_3$[57]. Because this model incorporates local symmetry-breaking distortions, it provides a more appropriate approximation for the thin-film domain-wall environment. This polarization is comparable to that predicted for ferroelastic twin walls in $CsPbI_3$ (6 μC cm^{-2})[51] but lower than the values calculated for $CaTiO_3$ (27.7 μC cm^{-2})[58] and $SrTiO_3$ (7.14 and 7.95 μC cm^{-2})[9] twin walls. Nevertheless, even a polarization of this magnitude can generate local electrostatic fields sufficient to influence charge-carrier transport, separation, and recombination. Unlike $RFeO_3$-type systems, $CsPbI_3$ has no magnetic sublattices, so magnetically induced polarization through spin-lattice coupling is not relevant[59]. However, ferroelastic twin induced polarization is a more general mechanism that can occur in both systems and has been observed in $GdFeO_3$[50].

Could these cation displacements be a consequence of a biaxial strain or the film thinness? Although biaxial strain can induce ferroelectricity in nominally non-ferroelectric thin films[60], such a mechanism would be expected to produce a more spatially extended polar response across the film. In contrast, the polar distortion observed here is highly localized at {110} ferroelastic twin walls that arise from local structural confinement rather than a global strain-induced ferroelectric phase. We prepared 200 nm-thick films on quartz, comparable to those used in optoelectronic studies, and observed consistent structural and photophysical properties across different film thicknesses (**Fig. S14-S16**). These PL and XRD measurements do not resolve the local atomic-structure of the twin walls, and we cannot apply atomic-resolution TEM to such thick films. We therefore do not establish experimentally that the twin wall polarization persists in 200 nm or in bulk $CsPbI_3$. However, first-principles calculations predict polar twin walls in bulk $CsPbI_3$[51], suggesting that such wall polarization may persist beyond the 35 nm thin films examined here. Persistence of the local polar distortion in thicker specimens therefore remains a hypothesis requiring direct experimental verification.

Different behavior applies to the {112}-type domain walls. In the orthorhombic domain interiors of $CsPbI_3$, the A-site Cs^+ cations exhibit alternating off-center displacements coupled to octahedral tilts, resulting in no net dipole in the regions away from the twin walls. At the {112}-type twin walls, this antipolar alternating pattern is disrupted due to the change in octahedral tilt sense across the wall, which drives the Cs atoms back to a central position (**Fig. 5B)**. Prior studies have shown that such antipolar A-site displacements in *Pbnm* perovskites inhibit ferroelectricity. Furthermore, in order to introduce polarization[42] it is necessary to suppress the Cs displacement, for example, by applying an external electric field. Although the closely spaced Cs atomic columns at the {110} twin walls cannot be clearly resolved and quantitatively measured, the apparent incompatibility between Cs displacement and polarization suggests that Cs displacement is likely suppressed also at {110} twin walls.

The distinction in polar behavior between the {110} and {112} twin walls originate from their differing atomic structures (**Fig. 5**). The {110} walls lie parallel to the octahedral framework (along <001>$_c$), intersecting the iodine columns at the octahedral corners. In contrast, the {112} walls intersect the octahedral network at ~ 45°, crossing through the center of the octahedra (along <011>$_c$). This structural difference imposes distinct constraints on the strain distribution and structural distortions at the twin wall, leading to different polarization behavior. Notably, theoretical calculations have predicted polarization at {112} twin walls in tetragonal $CsPbI_3$ and $SrTiO_3$ (space group *P4/mbm*), where only a single octahedral tilt mode is present[9,51]. These results underscore the critical role of octahedral tilts and A-site antipolar motion in governing the emergence or suppression of twin wall localized polarization.

We note that such {110} ferroelastic twin walls are not expected in all the photoactive halide perovskites, as their formation depends on symmetry and tilt distortions. For instance, in tetragonal phases (where a_t=b_t, "t" for tetragonal), only {112} ferroelastic twin walls have been reported, such

as those in $MAPbI_3$[16]. While in cubic $FAPbI_3$ (where a_c=b_c=c_c, "c" for cubic), only non-ferroelastic, face-sharing twin walls have been observed[61].

In summary, we employed low-dose atomic-resolution TEM to reveal and characterize twin domains and domain walls in orthorhombic $CsPbI_3$ thin films, structures not previously observed in this materials class. Importantly, we identify nanoscale polarization confined to {110} twin walls embedded within a non-polar thin film crystal matrix. Such polarized domain walls are known in perovskite oxides to enhance local conductivity and photovoltaic responses, enabling domain-wall-based nanoelectronics[10,62–64]. By revealing an analogous structural element in the halide perovskite of $CsPbI_3$, a key semiconductor for solar cells and light-emitting devices, our work translates oxide ferroic insight into the realm of halide perovskites.

Materials and Methods

$CsPbI_3$ thin-film sample fabrication. $CsPbI_3$ samples were fabricated directly on TEM grids (Agar scientific, Cu-400 mesh) through a previously reported vapor co-deposition method in our custom-built thermal evaporator[41]. An ultrathin, 3-nm carbon substrate was used to minimize background contrast during TEM imaging. Simultaneous deposition on z-cut quartz substrates can be used for correlative photophysical measurements, as demonstrated in our previously work on $CsPbI_3$ and related compounds[39,41]. Briefly, the chamber was pumped down to a base pressure below $3x10^{-6}$ mbar for all depositions, and precursors of CsI (Alfa-Aesar, 99.998% metals base) and PbI_2 (Alfa-Aesar, 99.998%, ultra-dry metals base) were used. As-deposited films were immediately annealed after deposition in N_2 atmosphere. Thin films deposition was controlled using quartz crystal microbalances positioned near the evaporation sources and substrate to monitor the precursor flux ratio and nominal film thickness. Based on our previously optimized protocol[39], the CsI:PbI_2 ratio was set to 1.25:1. The nominal film thickness was maintained at 35 nm to facilitate high-resolution TEM measurements. The substrate was kept at 20 °C and the walls of chamber was kept at 17 °C through two separate chillers. Prior to deposition, TEM grids were also O_2-plasma treated for 0.3 minutes. Film thickness was determined by concurrently depositing $CsPbI_3$ films on z-cut quartz substrates alongside the TEM-grid specimens, followed by measurement using a stylus profiler. Furthermore, the thickness of 35 nm was found to be consistent with measurements from electron diffraction (**Fig. S2**). For the sample transfer from Oxford, United Kingdom to Melbourne, Australia, the samples were stored and securely sealed inside a light-proof, stainless-steal transfer unit in N_2.

The nominal CsI:PbI_2 ratio of 1.25:1 is the precursor flux ratio monitored by the quartz crystal microbalances during co-deposition of CsI and PbI_2. It should not be interpreted as a direct measurement of the final film stoichiometry. However, the presence of a weak CsI secondary-phase reflection near 27.5° in addition to the dominant γ-$CsPbI_3$ (110) and (220) reflections in XRD patterns (**Fig. S15**) is indicative of residual unreacted CsI remaining, consistent with our aimed CsI-excess co-depositions. The atomic-resolution TEM measurements reported here were made in regions whose atomic structure determined from images and diffraction patterns are consistent with γ-$CsPbI_3$. The CsI has a structure of $pm\bar{3}m$ and hence is inconsistent with the measured crystal structure of the twin walls, although an indirect influence of the Cs-rich growth condition on defect or twin formation cannot be excluded.

Transmission electron microscopy (TEM). Scanning Transmission Electron Microscope - Annular Dark Field (STEM-ADF) images were taken using a Thermo Fisher Scientific Spectra φ Field Emission Gun Transmission Electron Microscopy (FEG-TEM) and a FEI Titan^3 80-300 FEG-TEM, both equipped with probe and imaging aberration correctors. Images were acquired at 300 kV accelerating voltage, using a 15 mrad probe-forming aperture, and 39-200 mrad detector collection angle. 4D-STEM datasets were collected using an electron microscope pixel array detector (EMPAD), with 256 x 256 probe positions, 128 x 128 pixel diffraction patterns acquired at 1 kHz, whereby a ~3.4 nm electron probe is scanned across the specimen. The total dose of a single 4D-STEM scan is estimated to be 14.6 e/Å^2.Four dimensional (4D)-STEM data sets were

analyzed using an in-house computer code developed by Dr Bryan Esser, called Quant4D. Quantitative analyses of the location of intensity maxima in STEM-ADF images were performed using an open-source Python package Atomap[65], where both the precise position and shape of atomic columns are measured using 2D elliptical Gaussian distributions. TEM specimens were transferred in a glove box from the light-proof, N_2-filled transfer unit and mounted on a single tilt holder into the vacuum of the TEM. All TEM experiments followed a "shoot blind" protocol whereby zero electron dose was applied to the region-of interest during the experiment set up, neither during zone axis tilting nor parameter tuning. Kinematic and dynamical diffraction pattern simulations were performed using SingleCrystal (**Fig. 2**) and MuSTEM (**Fig. S1**), respectively.

To obtain STEM-ADF images suitable for quantitative measurements while preserving the structural integrity of the material, the electron dose was minimized by using dose-fractionation: 20 frames were acquired, each with a dose calibrated using a direct-counting detector and set to 1500 e/Å^2. Frames were carefully inspected to confirm that no structural changes occur and then summed to increase the signal-to-noise ratio.

Data, Materials, and Software Availability

All relevant data generated in this study are provided in the paper and its Supplementary Information files. Source data has also been deposited in Figshare under the accession link: https://doi.org/10.6084/m9.figshare.32815910.

Acknowledgments

Financial support from the Australian Research Council (ARC) is appreciated. J.E. acknowledges ARC Laureate Fellowship FL220100202 and J.E. and M.B.J. acknowledge ARC Discovery Project DP200103070. The authors acknowledge use of facilities and support of staff within the Monash Centre for Electron Microscopy, a node of Microscopy Australia. The Thermo Fisher Scientific Spectra φ TEM was funded by ARC LE170100118 and the FEI Titan^3 80-300 FEG-TEM was funded by ARC LE0454166. M.B.J. acknowledge financial support from the Engineering and Physical Sciences Research Council (EPSRC).

References

1. Kojima, A., Teshima, K., Shirai, Y. & Miyasaka, T. Organometal halide perovskites as visible-light sensitizers for photovoltaic cells. *J. Am. Chem. Soc.* **131**, 6050–6051 (2009).

2. Shi, Y. *et al.* Ten Years of Perovskite Lasers. *Adv. Mater.* **2413559**, 1–37 (2025).

3. Veldhuis, S. A. *et al.* Perovskite Materials for Light-Emitting Diodes and Lasers. *Adv. Mater.* **28**, 6804–6834 (2016).

4. Dou, L. *et al.* Solution-processed hybrid perovskite photodetectors with high detectivity. *Nat. Commun.* **5**, (2014).

5. Yang, M., Kim, D. J. & Alexe, M. Flexo-photovoltaic effect. *Science* **360**, 904–907 (2018).

6. Zheng, H. & Loh, K. P. Ferroics in Hybrid Organic–Inorganic Perovskites: Fundamentals, Design Strategies, and Implementation. *Adv. Mater.* **36**, 1–18 (2024).

7. Nataf, G. F. *et al.* Domain-wall engineering and topological defects in ferroelectric and

ferroelastic materials. *Nat. Rev. Phys.* **2**, 634–648 (2020).

8. Meier, D. & Selbach, S. M. Ferroelectric domain walls for nanotechnology. *Nat. Rev. Mater.* **7**, 157–173 (2022).

9. He, R. *et al.* Ferroelastic Twin-Wall-Mediated Ferroelectriclike Behavior and Bulk Photovoltaic Effect in SrTiO3. *Phys. Rev. Lett.* **132**, 176801 (2024).

10. Sluka, T., Tagantsev, A. K., Bednyakov, P. & Setter, N. Free-electron gas at charged domain walls in insulating BaTiO3. *Nat. Commun.* **4**, (2013).

11. Qin, W. *et al.* Suppressing non-radiative recombination in metal halide perovskite solar cells by synergistic effect of ferroelasticity. *Nat. Commun.* **14**, 256 (2023).

12. Zhang, X., Wang, F., Zhang, B. Bin, Zha, G. & Jie, W. Ferroelastic Domains in a CsPbBr3 Single Crystal and Their Phase Transition Characteristics: An in Situ TEM Study. *Cryst. Growth Des.* **20**, 4585–4592 (2020).

13. Marçal, L. A. B. *et al.* In situ imaging of ferroelastic domain dynamics in CsPbBr3 perovskite nanowires by nanofocused scanning X-ray diffraction. *ACS Nano* **14**, 15973–15982 (2020).

14. Bari, M., Bokov, A. A., Leach, G. W. & Ye, Z. G. Ferroelastic Domains and Effects of Spontaneous Strain in Lead Halide Perovskite CsPbBr3. *Chem. Mater.* **35**, 6659–6670 (2023).

15. Strelcov, E. *et al.* CH3NH3PbI3 perovskites: Ferroelasticity revealed. *Sci. Adv.* **3**, e1602165 (2017).

16. Rothmann, M. U. *et al.* Direct observation of intrinsic twin domains in tetragonal CH3NH3PbI3. *Nat. Commun.* **8**, 6–13 (2017).

17. Liu, Y. *et al.* Chemical nature of ferroelastic twin domains in CH3NH3PbI3 perovskite. *Nat. Mater.* **17**, 1013–1019 (2018).

18. Röhm, H., Leonhard, T., Hoffmann, M. J. & Colsmann, A. Ferroelectric domains in methylammonium lead iodide perovskite thin-films. *Energy Environ. Sci.* **10**, 950–955 (2017).

19. Sharada, G. *et al.* Is CH3NH3PbI3 polar? *J. Phys. Chem. Lett.* **7**, 2412–2419 (2016).

20. Rakita, Y. *et al.* Tetragonal CH3NH3PbI3 is ferroelectric. *Proc. Natl. Acad. Sci. U. S. A.* **114**, E5504–E5512 (2017).

21. Fan, Z. *et al.* Ferroelectricity of CH3NH3PbI3 perovskite. *J. Phys. Chem. Lett.* **6**, 1155–1161 (2015).

22. Ambrosio, F., De Angelis, F. & Goñi, A. R. The Ferroelectric-Ferroelastic Debate about Metal Halide Perovskites. *J. Phys. Chem. Lett.* **13**, 7731–7740 (2022).

23. Röhm, H., Leonhard, T., Hoffmann, M. J. & Colsmann, A. Ferroelectric Poling of Methylammonium Lead Iodide Thin Films. *Adv. Funct. Mater.* **30**, (2020).

24. Kumar, A. *et al.* Atomic-resolution electron microscopy of nanoscale local structure in lead-based relaxor ferroelectrics. *Nat. Mater.* **20**, 62–67 (2021).

25. Li, W., Hao, M., Baktash, A., Wang, L. & Etheridge, J. The role of ion migration, octahedral tilt, and the A-site cation on the instability of Cs1-xFAxPbI3. *Nat. Commun.* **14**, 8523 (2023).

26. Rothmann, M. U. *et al.* Atomic-scale microstructure of metal halide perovskite. *Science* **370**, eabb5940 (2020).

27. Zhang, D. *et al.* Atomic-resolution transmission electron microscopy of electron beam–sensitive crystalline materials. *Science* **359**, 675–679 (2018).

28. Rothmann, M. U. *et al.* Structural and Chemical Changes to CH3NH3PbI3 Induced by Electron and Gallium Ion Beams. *Adv. Mater.* **30**, 1–7 (2018).

29. Zhang, J., Hodes, G., Jin, Z. & Liu, S. (Frank). All-Inorganic CsPbX3 Perovskite Solar Cells Progress and Prospects. *Angew. Chemie - Int. Ed.* **58**, 15596–15618 (2019).

30. Yang, S. *et al.* Ultra-High 1.27 V VOC of Pure CsPbI3 Perovskite Solar Cells with an Efficiency of 21.8%. *ACS Energy Lett.* **9**, 4817–4826 (2024).

31. Wang, J. *et al.* 21.15%-Efficiency and Stable γ -CsPbI3 Perovskite Solar Cells Enabled by an Acyloin Ligand. *Adv. Mater.* **35**, 2210223 (2023).

32. Fu, Y., Jin, S. & Zhu, X. Y. Stereochemical expression of ns 2 electron pairs in metal halide perovskites. *Nat. Rev. Chem.* **5**, 838–852 (2021).

33. Smith, E. H., Benedek, N. A. & Fennie, C. J. Interplay of Octahedral Rotations and Lone Pair Ferroelectricity in CsPbF3. *Inorg. Chem.* **54**, 8536–8543 (2015).

34. Marronnier, A. *et al.* Structural Instabilities Related to Highly Anharmonic Phonons in Halide Perovskites. *J. Phys. Chem. Lett.* **8**, 2659–2665 (2017).

35. Li, X. *et al.* Evidence for Ferroelectricity of All-Inorganic Perovskite CsPbBr3 Quantum Dots. *J. Am. Chem. Soc.* **142**, 3316–3320 (2020).

36. Sutton, R. J. *et al.* Cubic or Orthorhombic? Revealing the Crystal Structure of Metastable Black-Phase CsPbI3 by Theory and Experiment. *ACS Energy Lett.* **3**, 1787–1794 (2018).

37. Ma, M. *et al.* In situ imaging of the atomic phase transition dynamics in metal halide perovskites. *Nat. Commun.* **14**, 1–9 (2023).

38. Steele, J. A. *et al.* Thermal unequilibrium of strained black CsPbI3 thin films. *Science* **365**, 679–684 (2019).

39. Li, W. *et al.* Ruddlesden–Popper Defects Act as a Free Surface: Role in Formation and Photophysical Properties of CsPbI3. *Adv. Mater.* **2501788**, 1–13 (2025).

40. Liu, M., Johnston, M. B. & Snaith, H. J. Efficient planar heterojunction perovskite solar cells by vapour deposition. *Nature* **501**, 395–398 (2013).

41. Yuan, Q. *et al.* Control over the microstructure of vapor-deposited CsPbBr3 enhances amplified spontaneous emission. *Adv. Opt. Mater.* **13**, e02160 (2025).

42. Benedek, N. A. & Fennie, C. J. Why are there so few perovskite ferroelectrics? *J. Phys. Chem. C* **117**, 13339–13349 (2013).

43. Zhao, B. *et al.* Thermodynamically stable orthorhombic γ-CsPbI3 thin films for high

performance photovoltaics. *J. Am. Chem. Soc.* **140**, 11716–11725 (2018).

44. Wang, Y., Guyot, F., Yeganeh-Haeri, A. & Liebermann, R. C. Twinning in MgSiO3 Perovskite. *Science* **248**, 468–471 (1990).

45. Salje, E. K. H. & Ishibashi, Y. Mesoscopic structures in ferroelastic crystals: Needle twins and right-angled domains. *J. Phys. Condens. Matter* **8**, 8477–8495 (1996).

46. Salje, E. K. H. Ferroelastic materials. *Annu. Rev. Mater. Res.* **42**, 265–283 (2012).

47. Scott, C. A. M. & Bristowe, N. C. Universal Polar Instability in Highly Orthorhombic Perovskites. *J. Am. Chem. Soc.* **146**, 29735–29741 (2024).

48. Van Aert, S. *et al.* Direct observation of ferrielectricity at ferroelastic domain boundaries in CaTiO 3 by electron microscopy. *Adv. Mater.* **24**, 523–527 (2012).

49. Schiaffino, A. & Stengel, M. Macroscopic Polarization from Antiferrodistortive Cycloids in Ferroelastic SrTiO3. *Phys. Rev. Lett.* **119**, 1–5 (2017).

50. Ran, K. *et al.* Direct Visualization of Distorted Twin Boundaries in Ce-Doped GdFeO3. *Nano Lett.* **23**, 2945–2951 (2023).

51. Warwick, A. R., Íniguez, J., Haynes, P. D. & Bristowe, N. C. First-Principles Study of Ferroelastic Twins in Halide Perovskites. *J. Phys. Chem. Lett.* **10**, 1416–1421 (2019).

52. Whyte, J. R. & Gregg, J. M. A diode for ferroelectric domain-wall motion. *Nat. Commun.* **6**, 1–5 (2015).

53. Sharma, P. *et al.* Nonvolatile ferroelectric domain wall memory. *Sci. Adv.* **3**, e1700512 (2017).

54. Sanchez-santolino, G. *et al.* Resonant electron tunnelling assisted by charged domain walls in multiferroic tunnel junctions. *Nat. Nanotechnol.* **12**, (2017).

55. Salje, E. K. H., Li, S., Zhao, Z., Gumbsch, P. & Ding, X. Polar twin boundaries and nonconventional ferroelectric switching. *Appl. Phys. Lett.* **106**, (2015).

56. Sun, Y. *et al.* Subunit cell – level measurement of polarization in an individual polar vortex. *Sci. Adv.* **5**, eaav4355 (2019).

57. Zacharias, M., Volonakis, G., Giustino, F. & Even, J. Anharmonic lattice dynamics via the special displacement method. *Phys. Rev. B* **108**, 1–16 (2023).

58. Barone, P., Sante, D. Di & Picozzi, S. Improper origin of polar displacements at CaTiO 3 and CaMnO 3 Twin Walls. *Phys. Rev. B* **89**, 1–6 (2014).

59. Zhao, H. J., Bellaiche, L. & Chen, X. M. Improper electric polarization in simple perovskite oxides with two magnetic sublattices. *Nat. Commun.* **8**, 14025 (2017).

60. Haeni, J. H. *et al.* Room-temperature ferroelectricity in strained SrTiO3. *Nature* **430**, 583–586 (2004).

61. Li, W., Ding, S., Hao, M., Wang, L. & Etheridge, J. Discovery of Twin Defects in Hybrid Perovskite Nanocrystals: Atomic Structure and Impact on Photovoltaic Performance and Stability. *ACS Nano* **19**, 35037–35049 (2025).

62. Vasudevan, R. K. *et al.* Field enhancement of electronic conductance at ferroelectric

domain walls. *Nat. Commun.* **8**, 1–10 (2017).

63. Seidel, J. *et al.* Efficient photovoltaic current generation at ferroelectric domain walls. *Phys. Rev. Lett.* **107**, 1–4 (2011).

64. Chu, K. *et al.* Enhancement of the anisotropic photocurrent in ferroelectric oxides by strain gradients. *Nat. Nanotechnol.* **10**, 972–979 (2015).

65. Nord, M., Vullum, P. E., MacLaren, I., Tybell, T. & Holmestad, R. Atomap: a new software tool for the automated analysis of atomic resolution images using two-dimensional Gaussian fitting. *Adv. Struct. Chem. Imaging* **3**, 1–12 (2017).

Figure 1. Atomic position measurements in γ-$CsPI_3$ domain interiors. (A) Atomic model of orthorhombic γ-$CsPbI_3$ (*Pbnm* space group) with octahedral rotations described by the Glazer notation $a^-b^-c^+$, based on database ICSD-21955[43]. **(B)** Schematic illustrating the relationship between the orthorhombic ("ortho") unit cell and the cubic ("c") unit cell. **(C)** STEM-ADF image of a $CsPbI_3$ single crystal viewed along the [001] zone axis. **(D)** Enlarged view of the region marked in **(C)**. **(E)** Atomic structural model of orthorhombic phase $CsPbI_3$ viewed along the [001] zone axis. **(F)** Pb off-center displacement map derived from atomic-resolution STEM-ADF image in **(C)**, showing the degree of off-center displacement, if any, of Pb/I columns (red in **(D)**) relative to the geometric center of the four surrounding I columns (blue in **(D)**). **(G)** STEM-ADF image of a $CsPbI_3$ grain viewed along the [110] zone axis. **(H)** Enlarged view of the region marked in **(G)**. **(I)** Atomic structural model of orthorhombic phase $CsPbI_3$ viewed along the [110] zone axis. **(J)** Pb off-center displacement map derived from atomic-resolution STEM-ADF image in **(G)**, showing the degree of off-center displacement, if any, of Pb/I columns (red in **(H)**) relative to the center of the four surrounding Cs columns (green in **(H)**). Vectors in **(F)** and **(J)** indicate the direction and magnitude of Pb atom displacement from center.

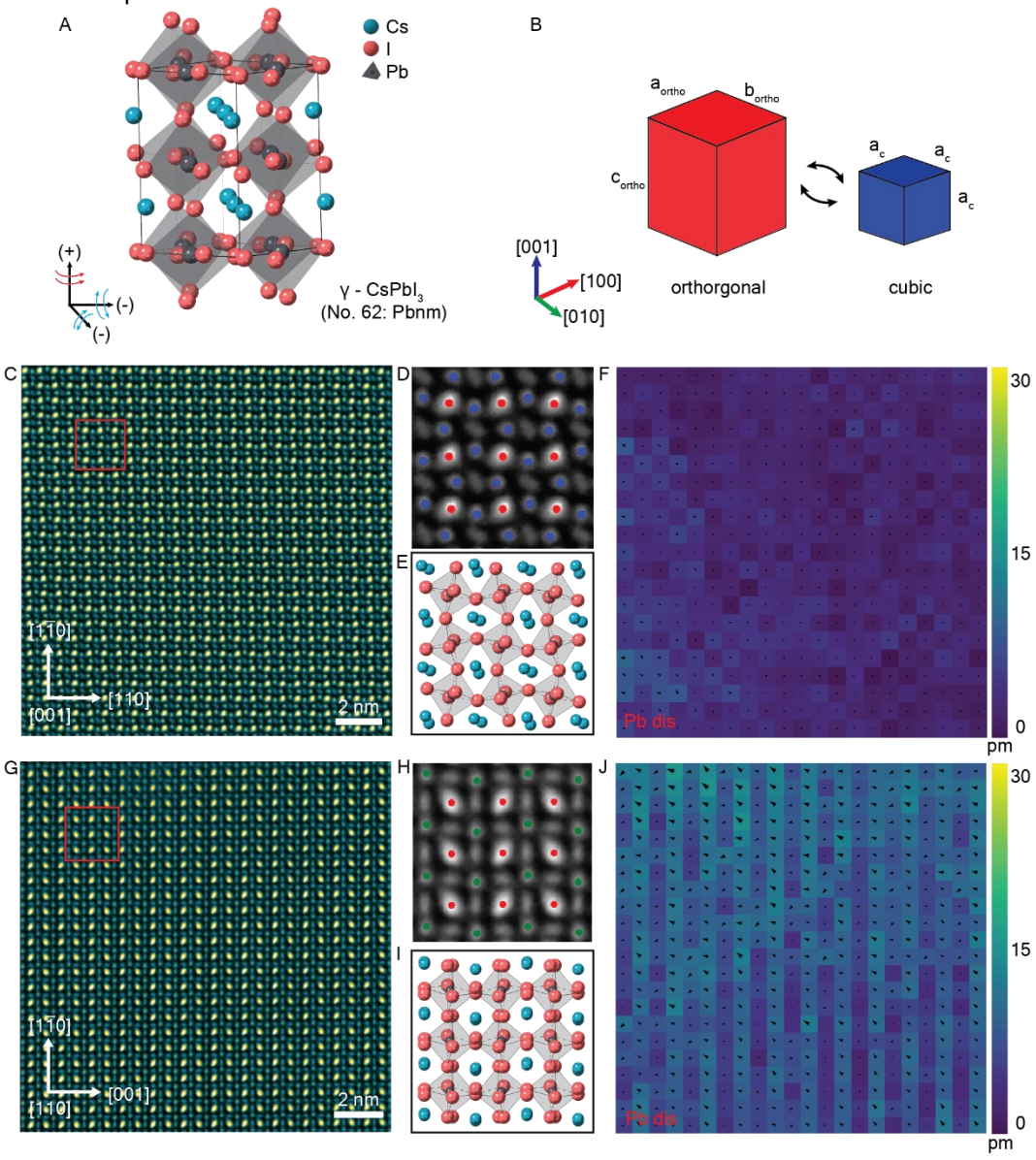


Figure 2. {110} twin domains in $CsPbI_3$. (A) TEM overview image of $CsPbI_3$ thin films. **(B)** HR-TEM image of a representative grain viewed along the [001] zone axis (red arrows point to twin domains). **(C)** Enlarged view of the domain region highlighted in **(B)**. **(D)** Fourier Transform of **(C)**. **(E)** Lattice parameter map of the region in **(C)** highlighting the consistent value of the lattice parameter within the domains but the rotation of lattice vector across the wall, derived from GPA of the circled spots **(D)**. **(F)** Schematic of the (110) twin wall crystallography, viewed along the [001] zone axis. **(G)** Simulated kinematic diffraction patterns of the A and B domains in **(F)**, with the overlaid pattern (A+B) at right. Squares indicate reflections kinematically forbidden by the crystal symmetry. Domains A and B correspond to regions with distinct crystal orientation. Image in (C) was generated by summing 150 frames of ultra-low-dose HR-TEM frames, each acquired at 2 e/Å^2, to preserve structural integrity and avoid beam damage (see **Fig. S7**).

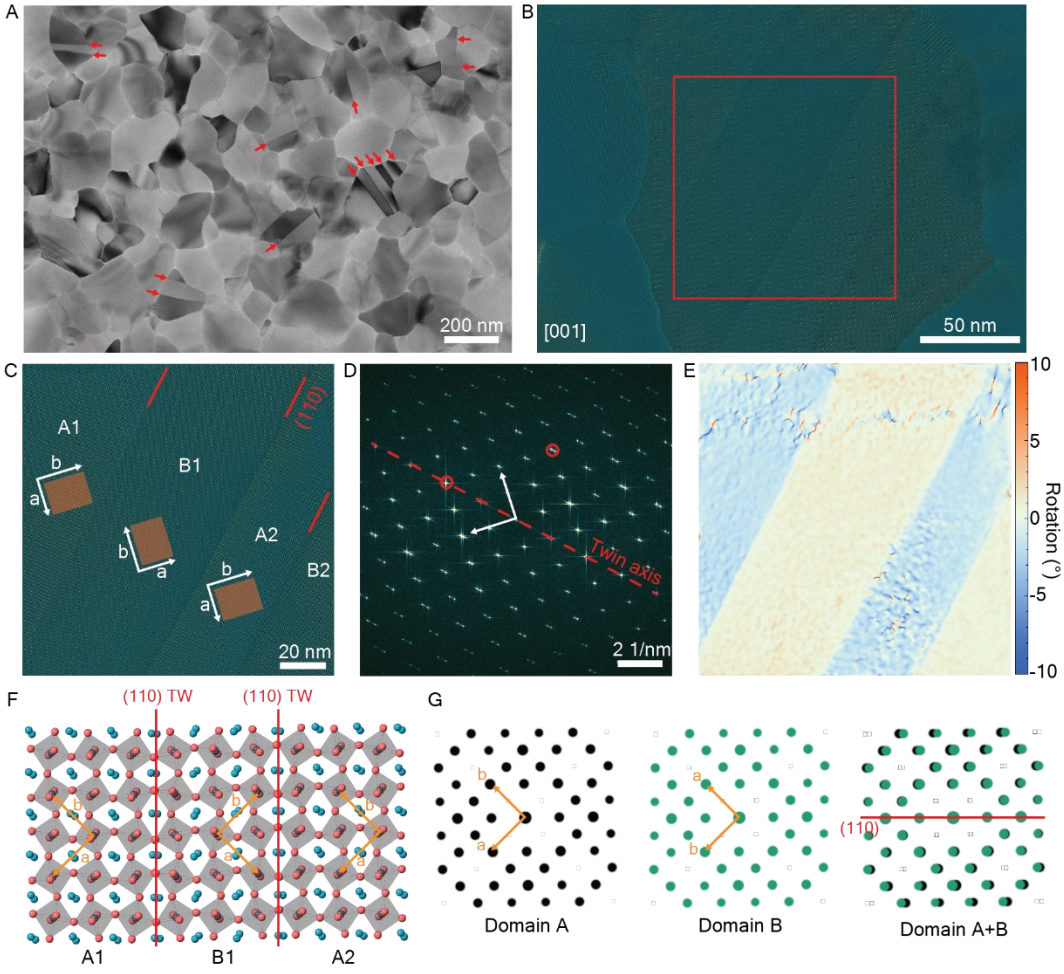


Figure. 3. Local polarization at the {110} twin wall. (A) Atomic-resolution STEM-ADF image of a [001]-oriented grain containing a (110) twin wall. **(B)** Ratio of Pb-Pb distances (*d1/d2*) across the twin wall, as illustrated in the inset. **(C)** Map of Pb/I column off-center displacements relative to the geometric center of the four surrounding I columns, as illustrated in the insert. Vectors represent the direction and magnitude of Pb off-center displacements. **(D)** Components of the Pb displacement vector resolved parallel and perpendicular to the twin wall, obtained by averaging the displacement map in **(C)**. (A slight mistilt of the crystal away from the zone axis leads to an off-set error of all displacement measurements. Therefore, background subtraction was applied to the line profiles, as shown in **Fig. S9**). vertical lines indicate the position of the twin wall.

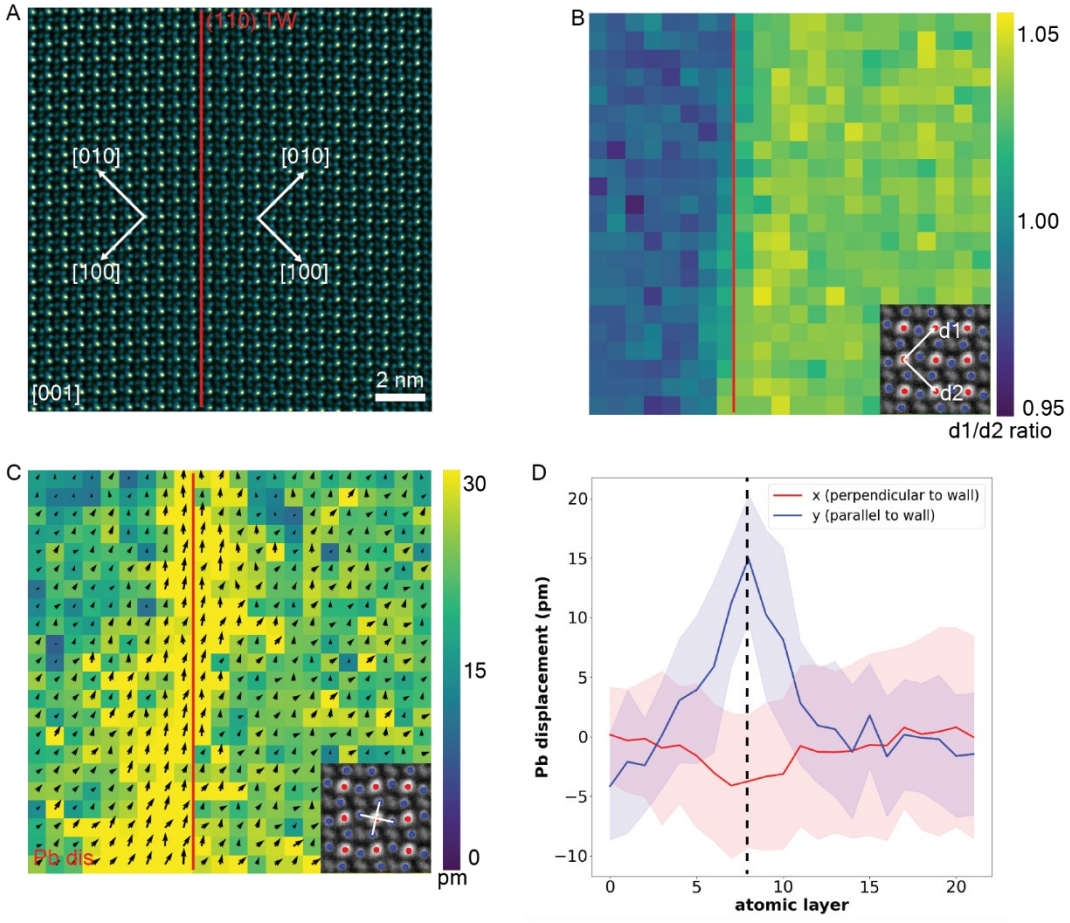


Figure 4. {112} ferroelastic twin wall. (A) Image of a [110]-oriented grain generated by integrating all pixel signals within each diffraction pattern of the acquired 4D-STEM dataset. **(B)** Averaged diffraction pattern from domain A. **(C)** Averaged diffraction from domain B. **(D)** STEM-ADF image of a representative {112} twin wall. **(E)** Map of Pb/I column off-center displacements relative to four surrounding Cs columns, as illustrated in the insert. Vectors indicate the direction and magnitude of Pb off-center displacements. **(F)** Map of Cs column off-center displacements relative to four surrounding Pb/I columns, as illustrated in the insert. Vectors indicate the direction and magnitude of the Cs off-center displacement. **(G)** Ellipticity vector map measured from Pb/I columns in **(D)**, a measure of octahedral tilt. The line direction indicates the orientation of the ellipse major axis. Line length and color indicate the magnitude of ellipticity (major axis/minor axis).

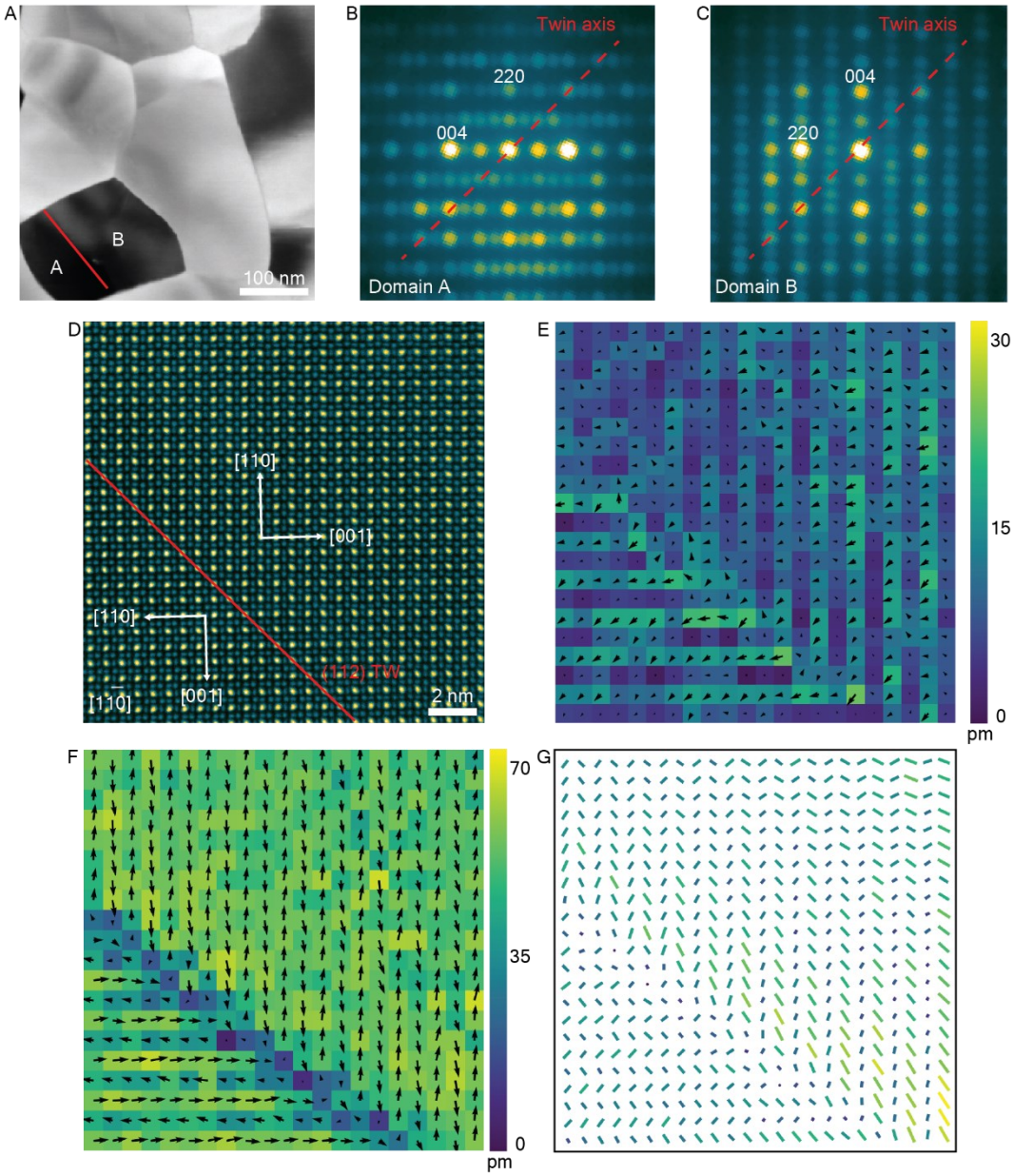


Figure 5. Schematics of twin walls in orthorhombic $CsPbI_3$. (A) Local polar displacement of Pb at the {110} twin wall. **(B)** Local suppression of octahedral tilts and Cs antipolar displacement at the {112} twin wall. **(C)** Schematic of polarized {110} twin walls embedded within the non-polar domain-interior lattice.

